A Numerical Simulation of Sea Ice Cover in Hudson Bay

JIA WANG,* L. A. MYSAK,** AND R. G. INGRAM

Department of Atmospheric and Oceanic Sciences and Centre for Climate and Global Change Research, McGill University, Montreal, Quebec, Canada

(Manuscript received 7 January 1993, in final form 15 February 1994)

ABSTRACT

Hibler's dynamic–thermodynamic sea ice model with viscous–plastic rheology is used to simulate the seasonal cycle of sea ice motion, thickness, compactness, and growth rate in Hudson Bay under monthly climatological atmospheric forcing and a prescribed ocean surface current field. The sea ice motion over most of the domain is driven mainly by the wind stress. Wintertime sea ice velocities are only of the order of 1–5 ($\times 10^{-4}$ m s^{-1}) due to the nearly solid ice cover and the closed boundary constraint of Hudson Bay. However, the velocities rise to 0.10–0.20 m s^{-1} during the melting and freezing seasons when there is partial ice cover. The simulated thickness distribution in mid-April, the time of heaviest ice cover, ranges from 1.3 m in James Bay to 1.7 m in the northern part of Hudson Bay, which compares favorably with observations. The area-averaged growth rate, computed from the model is 1.5–0.5 cm day^{-1} from December to March, is negative in May (indicative of melting) and reaches its minimum value of −4.2 cm day^{-1} (maximum melting rate) in July. During autumn, the main freezing season, the growth rate ranges from 1 to 2 cm day^{-1}. In the model, sea ice remains along the south shore of Hudson Bay in summer, as observed, even though the surface air temperatures are higher there than in central and northern Hudson Bay. A sensitivity experiment shows that this is mainly due to the pile-up of ice driven southward by the northwesterly winds. The simulated results for ice cover in other seasons also compare favorably with the observed climatology and with measurements from satellites. In particular, the model gives complete sea ice cover in winter and ice-free conditions in late summer. A series of sensitivity experiments in which the model parameters and external forcing are varied is also carried out.

1. Introduction

Numerical studies of the distribution and motion of sea ice in the Arctic have been carried out by Parkinson and Washington (1979), Hibler (1979, 1980), Hibler and Walsh (1982), Holland et al. (1991a,b; 1993), and many others. Furthermore, coupled ice–ocean models have been quite successful in studying large-scale sea ice characteristics (Hibler and Bryan 1987; Semtner 1987; Lemke et al. 1990; Fleming and Semtner 1991; Häkkinen and Mellor 1990; Piacsek et al. 1991; Riedlinger and Preller 1991; Cheng and Preller 1992). Also, to understand the ice motion in the Labrador Sea marginal ice zone (MIZ) and in the Bering Sea, two- and three-dimensional coupled ice–ocean models have been developed by Ikeda (1985, 1988, 1991a,b), Yao and Ikeda (1990), Tang (1991), Tang and Fissel (1991), and Overland and Pease (1988). One- and two-dimensional coupled ice–ocean models have been developed by Mellor and Kantha (1989) and Kantha and Mellor (1989) to study the sea ice dynamics in the MIZ of the Bering Sea. More recently, the three-dimensional simulation of deep water convection in the Greenland Sea has been carried out by Häkkinen et al. (1992).

Although sea ice modeling has been done for many regions, as described above, no detailed numerical study of sea ice cover in Hudson Bay has yet been carried out. The main purpose of this paper is to present the results of such a study. The probable reasons for the lack of previous modeling efforts on this topic include the following: 1) There is complete ice cover during winter, but during late summer Hudson Bay is ice free, which differs from the situation in the central Arctic and therefore presents new modeling challenges; 2) sea ice breaks up and melts during spring and forms during autumn, similar to the situation in other MIZs, which have proved difficult to model accurately in the past; and 3) due to its isolation, and hence limited field studies, the ocean circulation in Hudson Bay is poorly known and therefore there is little knowledge of the ocean forcing that is required for models of the ice motion.

Danielson (1969, 1971) investigated the seasonal variations of sea ice, surface heat budgets, and the at-

* Current affiliation: Bedford Institute of Oceanography, Dartmouth, Nova Scotia.

Corresponding author address: Prof. Lawrence A. Mysak, Dept. of Atmospheric and Oceanic Sciences and Centre for Climate and Global Change Research, McGill University, Montreal, Quebec H3A 2K6, Canada.
E-mail: Mysak@Zephyr.Meteo.McGill.Ca

mospheric conditions in Hudson Bay. Walsh and Johnson (1979a,b), Parkinson and Cavalieri (1989), Mysak and Manak (1989), and Parkinson (1991) studied the temporal and spatial variability of sea ice in the Arctic regions, including Hudson Bay. Wang (1993) and Wang et al. (1994a) analyzed monthly data of sea level pressure, sea ice concentration, surface air temperature, runoff, and sea ice thickness in Hudson Bay, Baffin Bay, and the Labrador Sea for the period of 1953–87 to determine the climatology and seasonal cycle of sea ice cover. Wang et al. also found that the interannual variability of sea ice cover in the study region is associated with both the Southern Oscillation and the North Atlantic Oscillation. The seasonal cycle of ice cover and the distribution of late winter/early spring ice thickness as determined from the data (Markham 1981; Prinsenberg 1988) will be compared with the simulation results presented in this paper.

Wang (1993) and Wang et al. (1994b) employed the Blumberg–Mellor three-dimensional, multilevel, baroclinic numerical ocean model (Blumberg and Mellor 1983, 1987) to simulate the winter and summer ocean general circulation in Hudson Bay. The ocean model outputs include surface circulation and elevation, which have been used to provide the oceanic forcing underneath the sea ice model used in this paper. We use the two-level sea ice model of Hibler (1979) to simulate the seasonal cycle of sea ice motion, thickness, concentration, and melting and freezing under the prescribed monthly climatological atmospheric and wintertime oceanic forcing. While there is no explicit snow cover on top of the ice, the effect (albedo) of snow cover is implicitly included in the calculation of the solar radiation during winter (Danielson 1969).

We describe briefly the sea ice model in section 2 and discuss the external (atmospheric and oceanic) forcing and model parameters in section 3. The simulation results for the seasonal cycle of sea ice cover are given in section 4, and we carry out a sensitivity study in section 5. We also present in section 5 the ice anomalies due to typical negative air temperature anomalies that are associated with the Southern Oscillation and the North Atlantic Oscillation (Wang et al. 1994a). The summary and conclusions are given in section 6.

2. Description of the model

The sea ice model we use has been described in Hibler (1979, 1980). We briefly present the governing equations and discuss some important details of the model below.

The two-dimensional momentum equation for sea ice motion in Cartesian coordinates takes the form

$$m\frac{D\mathbf{u}}{Dt} + mf\mathbf{k}\times\mathbf{u} - \mathbf{F} = \tau_a + \tau_w - mg\nabla\xi, \quad (1)$$

where m is the ice mass per unit area, $D/Dt = \partial/\partial t + u\partial/\partial x + v\partial/\partial y$, $\mathbf{u}$ is the horizontal ice velocity vector, f is the Coriolis parameter, $\mathbf{k}$ is the vertical normal unit vector, and $\mathbf{F}$ is the internal ice stress. The three terms on the right-hand side of Eq. (1) are the external forcing terms, consisting of τ_a and τ_w, the air and water stresses, and the gradient force due to the sloping sea surface.

The air and water stresses are defined as

$$\tau_a = \rho_a C_a|\mathbf{U}_a|(\mathbf{U}_a\cos\phi + \mathbf{k}\times\mathbf{U}_a\sin\phi), \quad (2)$$

$$\tau_w = \rho_w C_w|(\mathbf{U}_w - \mathbf{u})| \times [\mathbf{U}_w\cos\theta + \mathbf{k}\times(\mathbf{U}_w - \mathbf{u})\sin\theta], \quad (3)$$

where $\mathbf{U}_a$ is the surface wind, $\mathbf{U}_w$ is the surface ocean current, C_a and C_w are the air and water drag coefficients, ρ_a and ρ_w are the air and water densities, and ϕ and θ are the air and water turning angles, which are both set to zero because the correction in direction and magnitude has been made in the calculation of the surface wind using the scheme of Ramming and Kowalik (1980), and the surface ocean current is used rather than the geostrophic current.

The viscous–plastic constitutive law has been described by Hibler (1979). The internal stresses are

$$F_x = \frac{\partial}{\partial x}\left[\eta\left(\frac{\partial u}{\partial x} - \frac{\partial v}{\partial y}\right) + \zeta\left(\frac{\partial u}{\partial x} + \frac{\partial v}{\partial y}\right) - \frac{P}{2}\right] + \frac{\partial}{\partial y}\left[\eta\left(\frac{\partial u}{\partial y} + \frac{\partial v}{\partial x}\right)\right], \quad (4)$$

$$F_y = \frac{\partial}{\partial y}\left[-\eta\left(\frac{\partial u}{\partial x} - \frac{\partial v}{\partial y}\right) + \zeta\left(\frac{\partial u}{\partial y} + \frac{\partial v}{\partial y}\right) - \frac{P}{2}\right] + \frac{\partial}{\partial x}\left[\eta\left(\frac{\partial u}{\partial y} + \frac{\partial v}{\partial x}\right)\right], \quad (5)$$

where ζ and η, the normal and shear viscosities, are given by

$$\zeta = \frac{P}{2\Delta}, \quad \eta = \frac{\zeta}{e^2} = \frac{P}{2\Delta e^2}, \quad (6)$$

where P is the ice pressure and

$$\Delta = \left\{\left[\left(\frac{\partial u}{\partial x}\right)^2 + \left(\frac{\partial v}{\partial y}\right)^2\right]\left(1 + \frac{1}{e^2}\right) + \frac{4}{e^2}\left(\frac{\partial u}{\partial y} + \frac{\partial v}{\partial x}\right)^2 + 2\frac{\partial u}{\partial x}\frac{\partial v}{\partial y}\left(1 - \frac{1}{e^2}\right)\right\}^{1/2} \quad (7)$$

in which $e = 2$ is the ratio of principal axes of the ellipse. It is noted that besides the divergence term $\zeta(\partial u/\partial x + \partial v/\partial y)$ and pure pressure term $P/2$ in the square brackets of Eqs. (4) and (5), there are two other terms, $\eta(\partial u/\partial x - \partial v/\partial y)$ (stretching) and $\eta(\partial u/\partial y + \partial v/\partial x)$ (compression), which uniquely characterize the sea ice internal stresses in the viscous–plastic manner. This constitutive law relates internal ice stress to

ice deformation and ice strength. This rheology allows ice to flow plastically for normal strain rates and to deform in a linear viscous manner for small strain rates. The nonlinear normal and shear viscosities used in the ice rheology are set to have the maximum values $\zeta_{\max} = (2.5 \times 10^8)P$ and $\eta_{\max} = \zeta_{\max}/e^2$. These limiting values are used to avoid numerical instability when ice strain rates are very small.

To couple the ice strength to the ice thickness characteristics, the ice pressure P takes the form

$$P = P^* h \exp[-C(1 - A)], \tag{8}$$

where P^* (ice strength) and C (ice strength decay constant) are empirical constants and A is the compactness (ice concentration). This formulation makes the strength strongly dependent on the amount of thin ice (characterized by $1 - A$), while it also allows the ice to strengthen as it becomes thicker, as measured by the thickness h.

To simulate both dynamic and thermodynamic effects, two ice categories, thick and thin, are used with a cutoff thickness of $h_0 = 0.5$ m for the thin ice. The goal is to have the open water represented approximately by the combined fraction of both open water and thin ice up to the cutoff thickness h_0. This ice-thickness model (Hibler 1980, Appendix B), with both dynamics and thermodynamics considered, is similar to the "zero-layer" thermodynamic ice model of Semtner (1976). In this study, the snow cover is neglected due to lack of any detailed data. The ice compactness A is defined as the fractional area within a grid cell covered by thick ice, while $(1 - A)$ is the fractional area covered by the thin ice and open water. The continuity equations for thickness and compactness are given by

$$\frac{\partial h}{\partial t} = -\nabla \cdot (\mathbf{u}h) + D_{iff} + S_h, \tag{9}$$

$$\frac{\partial A}{\partial t} = -\nabla \cdot (\mathbf{u}A) + D_{iff} + S_A, \tag{10}$$

where $A \leq 1$, S_h and S_A are the thermodynamic forcing or source terms, and D_{iff} is the horizontal diffusion term, which is essential for numerical stability. $D_{iff}(h, A) = D_1 \nabla^2(h, A) + D_2 \nabla^4(h, A)$, where ∇^2 is the horizontal Laplacian operator, and D_1 and D_2 are constants given in Table 1 (Hibler 1979).

The thermodynamic source term S_h for ice melt and growth is taken to be a linear combination of the fraction $(1 - A)$ of thin ice and the fraction A of thick ice:

$$S_h = -\frac{(1 - A)Q_{\text{air}} + AQ_{\text{ice}} + Q_{\text{sea}}}{\rho_{\text{ice}} L_f}, \tag{11}$$

where Q_{air} is the net incoming atmospheric heat flux at the surface of the open water or leads due to shortwave solar radiation, longwave radiation, sensible and latent heat fluxes; Q_{ice} is the conductive heat flux through the ice into the ocean; Q_{sea} is the oceanic heat flux transported into the oceanic mixed layer from the deep ocean or the heat flux due to the heat content of the basin; L_f is the latent heat of fusion of sea water; and ρ_{ice} is the ice density. Sea ice tends to grow (melt) when $S_h > 0$ (<0), since the ice loses (gains) heat.

TABLE 1. Model parameters used in the control run.

Parameter	Value
Air drag coefficient	$C_a = 0.0012$
Water drag coefficient	$C_w = 0.0055$
Decay constant	$C = 10.0$
Melting coefficient	$C_m = 2.0$
Water specific heat	$C_{p,w} = 3930$ J kg^{-1} K^{-1}
Yield curve eccentricity	$e = 2$
Coriolis parameter	$f = 2\Omega \sin\varphi$ s^{-1}
Cutoff ice thickness	$h_0 = 0.5$ m
Mixed layer depth	$h_w = 25$ m
Ice conductivity	$k_i = 2$ W m^{-1} K^{-1}
Latent heat fusion	$L_f = 3.34 \times 10^5$ J kg^{-1}
Air density	$\rho_a = 1.3$ kg m^{-3}
Ice density	$\rho_i = 910$ kg m^{-3}
Water density	$\rho_w = 1025$ kg m^{-3}
Ice strength	$P^* = 27 \times 10^3$ N m^{-2}
Grid spacing	$\Delta x = \Delta y = 55$ km
Time step	$\Delta t = 12$ hours
Max nonlinear normal viscosity of ice	$\zeta_{\max} = (P/4) \times 10^9$ kg s^{-1}
Max nonlinear shear viscosity of ice	$\eta_{\max} = \zeta_{\max}/e^2$
Wind and current turning angles	$\phi = \theta = 0$
Harmonic and biharmonic diffusion	$D_1 = 0.004\Delta x$, $D_2 = D_1 \Delta x^2$

The surface heat budget has been described in detail by Hibler (1980, Appendix B), following Parkinson and Washington (1979) and Manabe et al. (1979). The source term S_A for compactness is given by

$$S_A = \begin{cases} \dfrac{S_h}{h_0}(1 - A), & \text{if } S_h > 0 \quad \text{(growth)} \\ C_m \dfrac{S_h}{2h} A, & \text{if } S_h < 0 \quad \text{(melt)}, \end{cases} \tag{12}$$

where h_0 is the cutoff thickness between the thick and thin ice, C_m is the melting coefficient (the rate of conversion of ice-covered ocean to open water). In the Arctic sea ice simulation, Hibler (1979) used $C_m = 1$, because sea ice exists year long. Usually, open water rapidly forms (i.e., sea ice melts) in summer in Hudson Bay, giving completely open water in late summer. Thus, we choose $C_m = 2$ in the control run, a value that gives model results in good agreement with the observations. In practice, the freezing and melting terms in Eq. (12) are equally important in Hudson Bay, which differs from the Arctic Ocean where the melting term is of less importance and accounts for only a few percent of the open water formed in summer (Hibler 1979).

We include the oceanic mixed layer temperature T in the ice model and calculate it prognostically. When

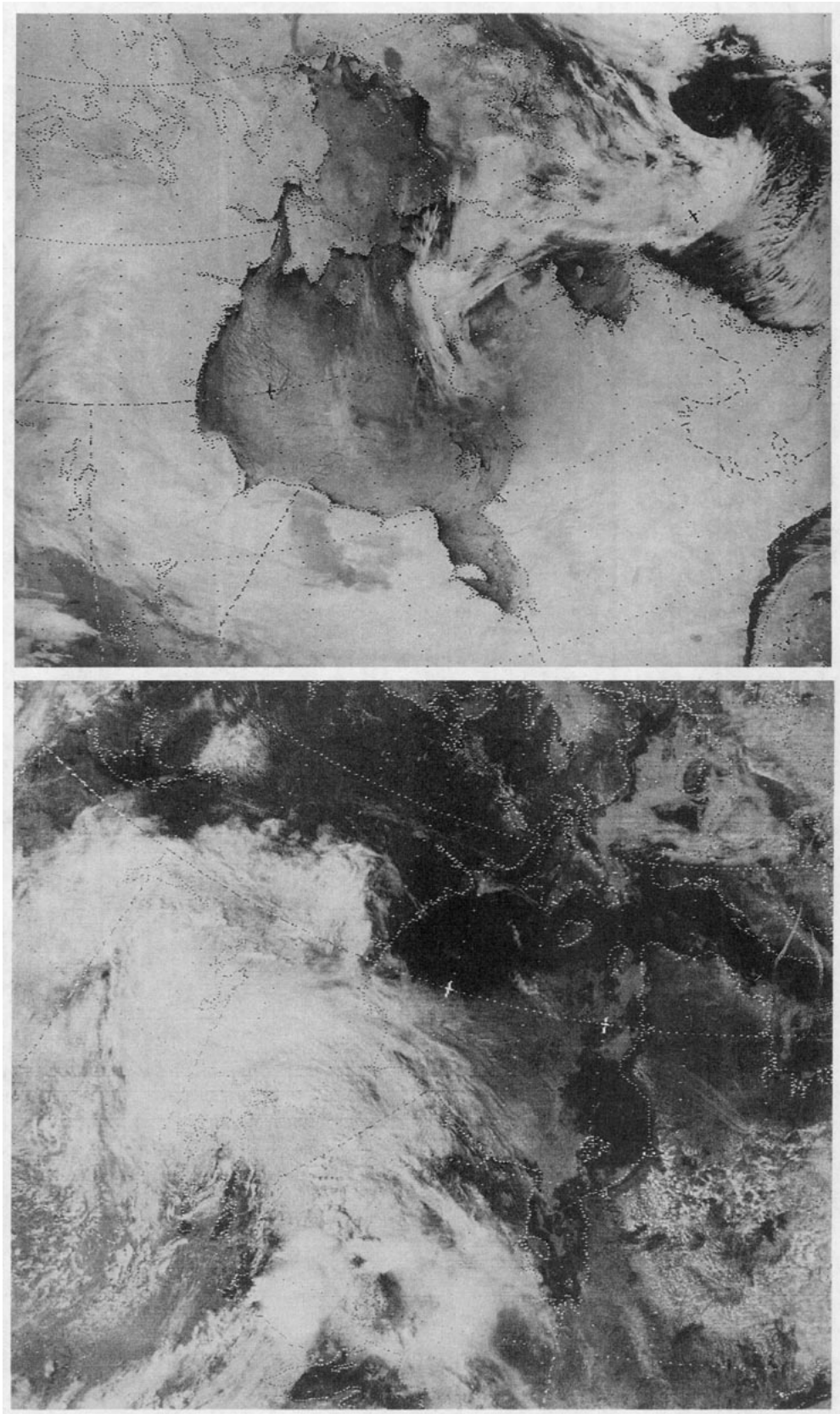

FIG. 1. NOAA satellite images of sea ice cover on 3 Jan (a: top) and 5 July (b: bottom) 1986.

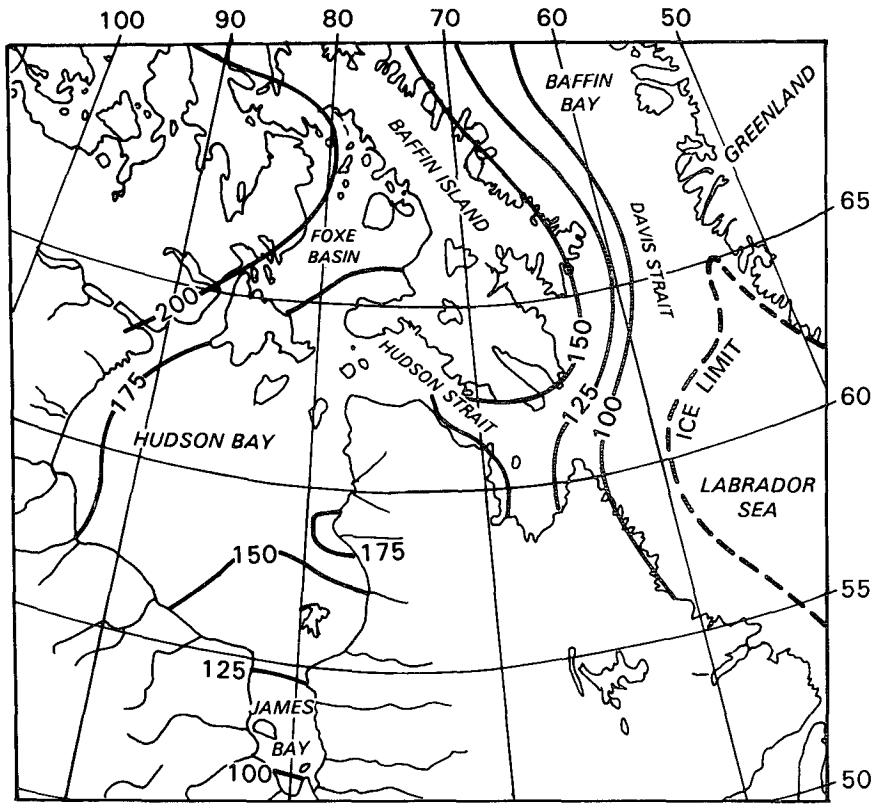

FIG. 2. Maximum sea ice thicknesses (cm) for eastern Canada (from Markham 1981; Prinsenberg 1988).

ice exists, T is set to the freezing temperature (−1.8°C); when there is no ice, it is calculated from

$$\frac{\partial T}{\partial t} = \frac{Q_{\text{air}} + Q_{\text{sea}}}{\rho_w C_{p,w} h_w}, \tag{13}$$

where ρ_w is the water density, $C_{p,w}$ is the specific heat of sea water, and h_w is the mixed layer thickness, which is set to 25 m everywhere in Hudson Bay (cf. Wang et al. 1994b). The salt flux is neglected when sea ice melts or grows. The modeling of the mixed layer temperature is essential for the simulation of the seasonal cycle in Hudson Bay, since there are ice-free conditions in August and September. When sea ice in any grid cell melts to zero concentration, we use Eq. (13) to calculate the mixed layer temperature at the grid cell. During the freezing season, the sea ice starts to form only after the modeled mixed layer temperature has dropped to the freezing point at the grid cell.

3. Observations, external forcing and model parameters

Figure 1 shows NOAA images of sea ice cover in Hudson Bay in January and July 1986. There is almost complete sea ice cover in January; near the northwest coast some leads exist due to strong northwesterly winds. Complete ice cover generally exists from February to April (not shown), with an average thickness of 1.5 m (Prinsenberg 1988). The sea ice starts to break up in James Bay and along the Hudson Bay coast in May. It piles up along the south shore of Hudson Bay from early July (Fig. 1b) to early August. From Fig. 1b, we observe that some ice is advected to the northeastern corner of the bay. In late August and September, there are ice-free conditions. In October and November, sea ice forms from north to south with some leads existing along the northwest coast. The spatial distribution of maximum sea ice thickness in Hudson Bay, which occurs in late winter/early spring, is shown in Fig. 2.

Figure 3 shows the net total surface heat budget in January, April, July, and October (after Danielson 1969). In January and April, the negative values indicate heat loss from the ice-ocean system to the atmosphere. The relatively small values indicate the insulating effect due to sea ice cover. From May to September (May, June, August, and September not shown), the heat flux is positive with a maximum in July (Fig. 3). From October to December (November and December not shown), the heat flux is again negative, indicating a heat loss from the ocean to the atmosphere. According to Markham (1981)

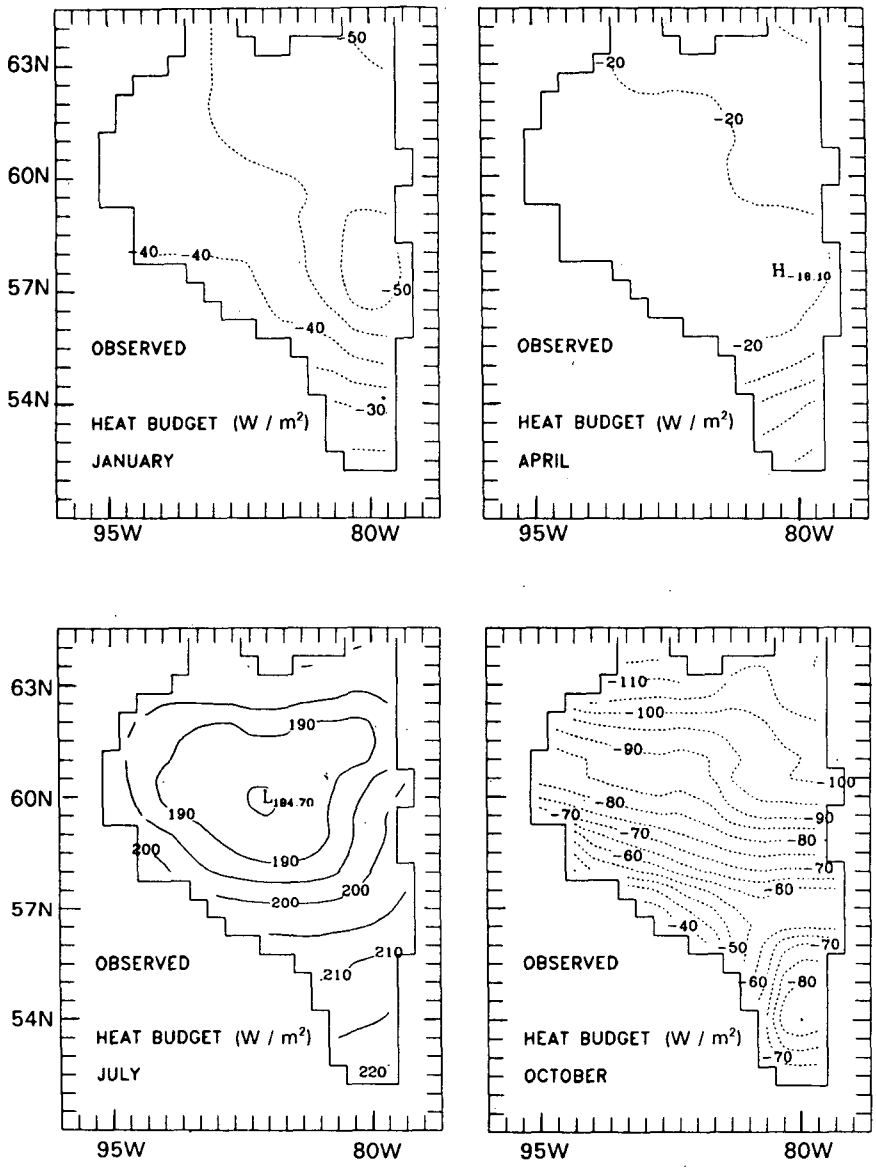

FIG. 3. The monthly climatology of surface heat budgets for each season (after Danielson 1969). Contour interval is 5 W m^{-2}. The positive (negative) values denote that the surface gains (loses) heat.

and Prinsenberg (1988), the freezing season starts in October.

Figure 4 shows the surface wind fields in January, April, July, and October, which were calculated from the monthly sea level pressure dataset of J. Walsh (Walsh and Chapman 1990; Wang et al. 1994a). A correction in magnitude and direction has been made using the scheme of Ramming and Kowalik (1980, chapter 1). In January, northwesterly winds prevail over the entire region, with a typical magnitude of 5–7 m s^{-1}. In April, the wind is mainly from the north. In summer, the northerly wind dominates in the northern portion of the domain, while a westerly wind prevails in the southern portion and in James Bay. The magnitude is typically 3–5 m s^{-1}. In October, the wind field is similar to that of summer. The magnitude gradually increases from October to December (not shown).

Figure 5 shows the typical surface winter current and elevation, which were derived by Wang (1993) from a three-dimensional ocean model (Blumberg and Mellor 1983, 1987). The model used 15 levels in the vertical and the same climatological atmospheric forcing as shown in Figs. 3 and 4 except for winter: December–February. A specified oceanic inflow (0.2 Sv) and outflow (0.3 Sv) (Sv $\equiv 10^6$ m^3 s^{-1}) together with

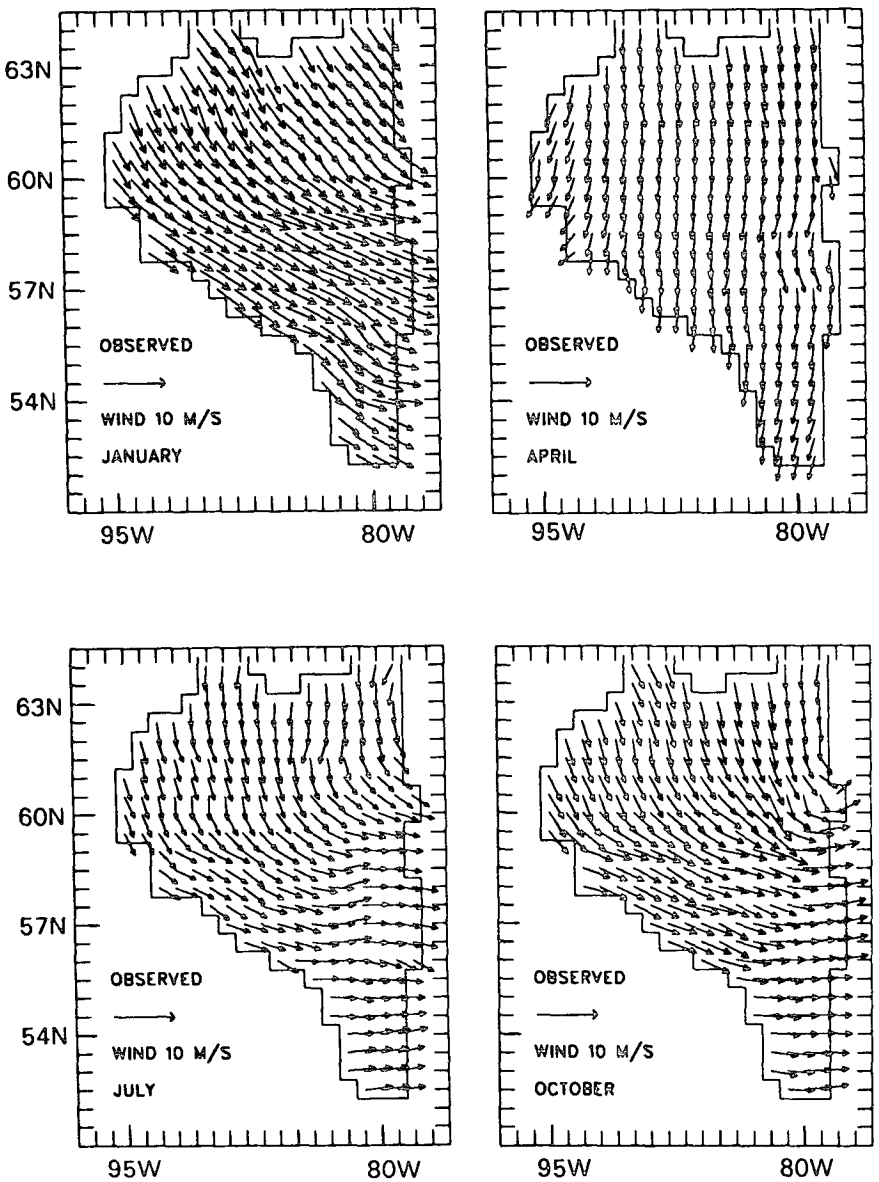

FIG. 4. The monthly climatology of surface wind fields for each season, which were calculated from the NCAR sea level pressure of the J. Walsh dataset (Walsh and Chapman 1990).

an appropriate radiation boundary condition were applied to the open boundaries (Wang 1993; Wang et al. 1994b). We note that the circulation is cyclonic in the surface layer, with an inflow from Roes Welcome Sound (in the northwest corner) and an outflow into Hudson Strait. The simulation results are in general agreement with the observations of Prinsenberg (1986). The central depression in the surface elevation is consistent with the cyclonic pattern of the surface circulation. The summer circulation obtained by Wang (1993) is stronger and also cyclonic, but it would have little effect on the ice flow because there are mainly ice-free conditions in summer. The circulation in spring and autumn cannot be simulated by an ocean-only model because there are no observed climatological surface temperature and salinity distributions, which are needed to force the model.

Monthly atmospheric forcing, part of which was shown in Figs. 3 and 4, was used to drive the ice model over a seasonal cycle. However, to simplify the calculations and since Hudson Bay is ice covered for over half the year (Nov–Jun), the surface ocean current and elevation fields were fixed throughout the year to those shown in Fig. 5 (typical of the wintertime circulation). The upward ocean heat flux into the mixed layer is believed to be small, due to the small heat con-

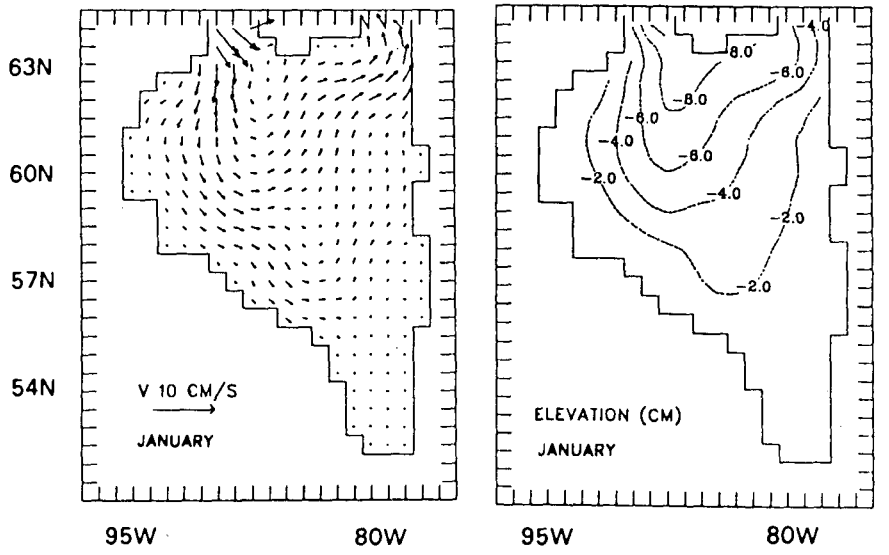

FIG. 5. The January (winter) surface circulation (left) and elevation (right), as derived from the output of the Blumberg–Mellor three-dimensional numerical model.

tent of the water in Hudson Bay during winter (Danielson 1969). Thus, we set the ocean heat flux to 2 W m^{-2} everywhere for all seasons. However, the mixed layer temperature is calculated by Eq. (13). The freezing temperature is assumed to be −1.8°C rather than specified as a function of salinity, because there are almost no surface salinity observations in winter, spring, and autumn. The monthly surface air temperature, solar radiation, longwave radiation, and latent and sensible heat fluxes were taken from a 1944–66 climatology documented by Danielson (1969). During winter and spring, the values of these quantities implicitly account for snow cover on the ice. The monthly air relative humidity data were taken from a 1951–60 climatology obtained by Titus (1967). These data were derived from station records, ship reports, and other sources (for details, see Danielson 1969).

The simulation domain is identical to that used in the ocean model (Wang 1993) and consists of a region divided into 24 × 27 grids, giving a coarse resolution of 55 km × 55 km. The integration time step is 12 hours. The ice model parameters for the control run are given in Table 1.

An initial thickness of 1 m was assumed everywhere on January 1, which is similar to the winter climatological value (Prinsenberg 1986); the compactness was set equal to 1. The initial ice velocities were $(u, v) = (0.01, -0.01)$ m s^{-1}. The ocean mixed layer temperature was set equal to the freezing point. The normal zero gradient boundary condition (i.e., extrapolation of the value next to the open boundary to the open boundary grid) is applied to all variables. This condition was also used by Yao and Ikeda (1990) in their simulation of the MIZ in the Labrador Sea. This type of boundary condition has been widely used in ocean modeling. The model was integrated for four years under the same climatological monthly atmospheric forcing and ocean forcing shown in Fig. 5. From Fig. 6, we see that the cycles of ice thickness and ice cover are repeated regularly each year. There are ice-free conditions in summer and a complete ice cover in winter and spring. The second-year output is used for the discussion below.

4. Results of the simulation

In this section, we discuss the seasonal variations of sea ice flow, areal cover, thickness, and growth rate

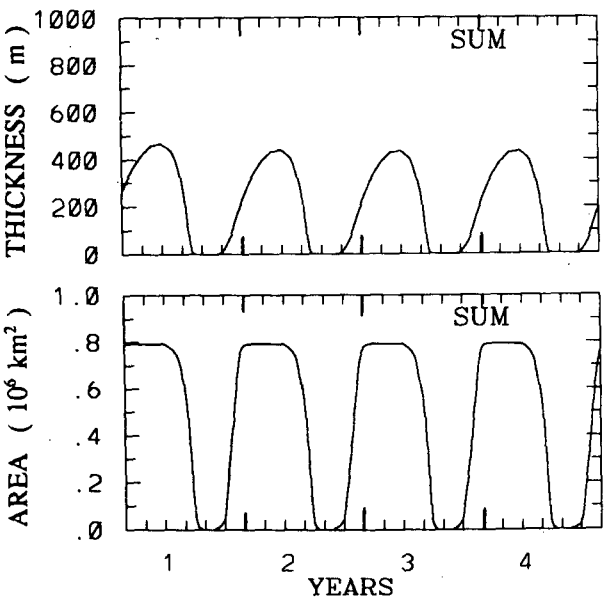

FIG. 6. The 4-year time series of the areal (gridpoint) sum of sea ice thickness and ice cover area for the control run.

from the control run. The sensitivity experiments will be given in the next section.

a. Seasonal cycle

Figure 7 (panels a, b, c, and e) shows the seasonal cycle of the area-averaged mixed layer temperature, sea ice kinetic energy per unit mass, thickness, and growth rate and, in panel d, the areal ice cover for the control run. The oceanic mixed layer temperature is at the freezing point from January to mid-June due to the presence of the ice cover and starts to rise to its maximum (about 4°C) by the end of August. In September, the area-averaged mixed layer temperature remains constant because the area-averaged surface heat budget is near zero. Starting in October, the mixed layer temperature starts to fall and drops to the freezing point at the end of December. At this latter time, sea ice covers most of Hudson Bay.

The kinetic energy of the sea ice (second panel) is relatively large only in the melting (spring) and freezing (autumn) seasons, with higher values occurring in autumn because of stronger winds. These results are not typical of the Arctic or the Greenland Sea MIZ, where the largest kinetic energies occur during wintertime (e.g., Holland et al. 1993).

The sea ice reaches its maximum thickness (1.6 m) in April and begins to break up in May (see third panel). During August and September, Hudson Bay is ice free. Sea ice starts to form in October, and there is almost complete ice cover by December. The simulated sea ice area (solid curve in fourth panel) compares favorably with the observations (dashed curve). The sea ice area is constant from January to April due to the boundary constraint (Parkinson and Cavalieri 1989; Wang et al. 1994a). This boundary constraint, which is absent in the Labrador Sea, Greenland Sea, and the Arctic Ocean, occurs because of the almost-closed coastline around Hudson Bay. Thus, once Hudson Bay is frozen over (in January), the sea ice area remains constant until May; however, the sea ice thickness keeps increasing, as shown in Fig. 7 (cf. panels c and d).

From January to April, the area-averaged growth rate decreases from 1.5 to 0 cm day^{-1} (panel e in Fig. 7). From May to mid-July, the negative values indicate ice melting, with a maximum melting rate of 4.2 cm day^{-1} in the middle of July. From August to early October, the growth rate is zero, since during this time there is no ice in Hudson Bay. From late October to December, the average growth rate is about 1–2 cm day^{-1}.

Figure 8 shows the spatial pattern of sea ice velocity in mid-January (day 15), mid-April (day 105), mid-July (day 195), and mid-November (day 315). We note that in most of Hudson Bay, the sea ice motion follows the northwesterly winds (see Fig. 4) in mid-January and mid-April; however, in the northeastern

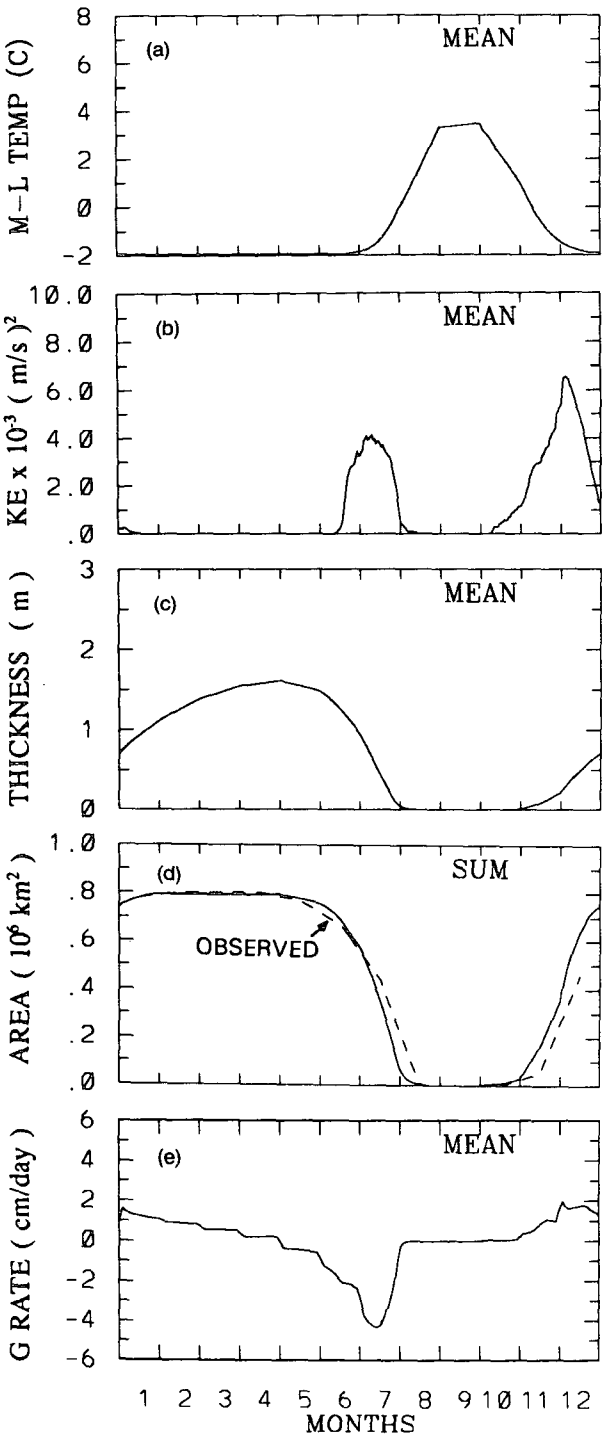

FIG. 7. The seasonal cycle of the area-averaged oceanic mixed layer temperature (a), kinetic energy per unit mass (b), thickness (c), and growth rate (e). Panel d shows the seasonal cycle of areal ice cover; the dashed curve is the observed areal ice cover derived from the monthly sea ice concentration supplied by J. Walsh (Walsh and Johnson 1979a).

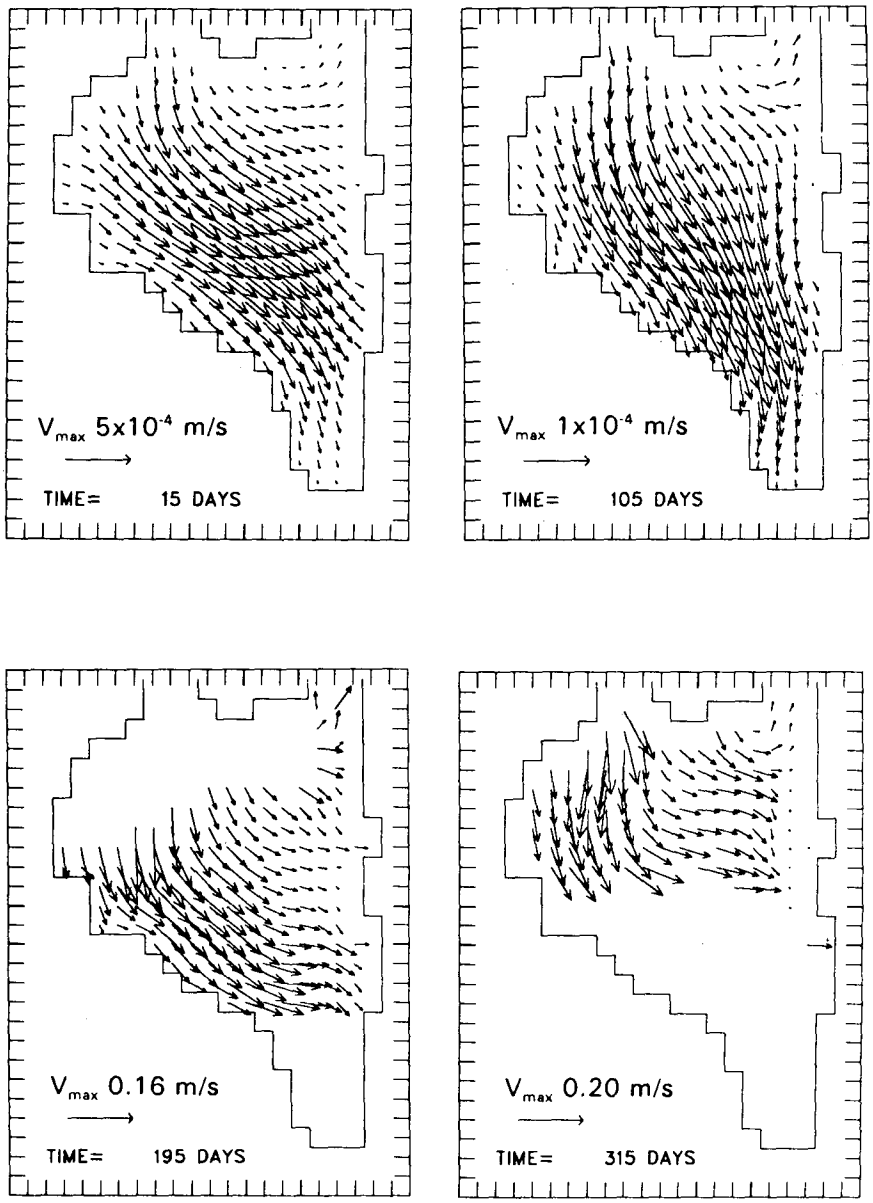

FIG. 8. The sea ice velocity fields in mid-Jan (day 15), mid-Apr (day 105), mid-Jul (day 195), and mid-Nov (day 315) for the control run. Note that the maximum velocity vector in each panel is different: 5×10^{-4}, 1×10^{-4}, 0.16, and 0.20 m s^{-1}, respectively, for day 15, 105, 195, and 315.

part of the domain, the sea ice is exported out of the bay because of the ocean circulation (see Fig. 5). Maximum velocities are 5×10^{-4} m s^{-1} in mid-January and 1×10^{-4} m s^{-1} in mid-April, since sea ice becomes thicker in spring. By mid-July (day 195), sea ice accumulates mainly along the south and east coasts. The presence of ice in the latter region during July is not in accord with observations, which show this to be an ice-free region (Fig. 1b). The maximum velocity in July is 0.16 m s^{-1}. In mid-November (day 315), the sea ice follows the wind and current directions in the northern part of the bay; the maximum velocity is 0.20 m s^{-1}. The velocities during the melting and freezing seasons are comparable to those observed over the shelf off Labrador and Newfoundland (about 0.20 m s^{-1}) (Prinsenberg and Peterson 1992).

Figure 9 shows the seasonal cycle of the horizontal distribution of the control-run thickness. The sea ice is 1 m thick in mid-January, increasing to 1.3–1.7 m in mid-April, with a well-defined south–north gradient, which is quantitatively consistent with the observations shown in Fig. 2. By mid-July (day 195), the ice thickness decreases to less than 0.9 m. The relatively heavy ice conditions along the south coast are presumably

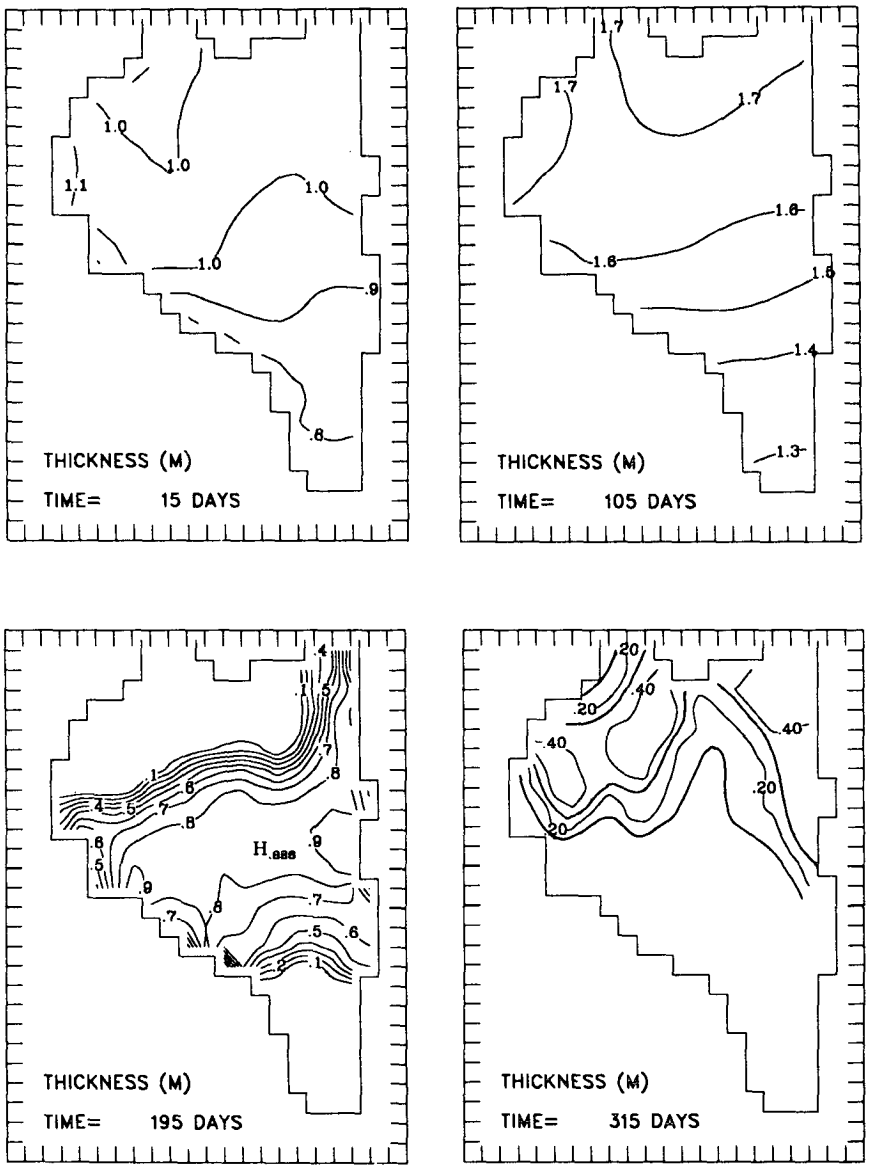

FIG. 9. As in Fig. 8 except for thickness. Contour interval is 0.1 m.

due to the ice being pushed southward by the northwesterly winds. However, according to observations there should be no heavy ice along the eastern shore in mid-July. This discrepancy will be discussed later. In mid-November (day 315), the thickest ice is located in the northern part of the domain. Along the northwestern coast, the small ice thickness in November indicates the presence of leads, created by the strong northwesterly winds in this season.

The compactness distributions in mid-July and mid-November will be discussed in section 4b. But we mention here that during winter and spring, there is complete ice cover. Figure 10 shows the spatial distributions of growth rate in mid-July and mid-November. The decay rate reaches its maximum in mid-July (left panel), with the area-averaged value being about 4 cm day^{-1}. During the freezing season (day 315), the growth rate is around 2–3 cm day^{-1} (right panel). In mid-January and mid-April, the growth rates (not shown) are about 1.5 and 0.5 cm day^{-1}, respectively.

In summary, the model reproduces seasonal cycles of sea ice cover and thickness that compare favorably with observations. Although there are no observations of ice velocity, the modeled results seem reasonable. However, one discrepancy we note is that in mid-July (day 195), the sea ice does not melt along the east coast (see Figs. 8–10). The observations (Fig. 1b) show ice-free conditions there. This may be because the ocean heat flux is fixed everywhere, whereas in reality it varies spatially. Prinsenberg (1984) also showed that

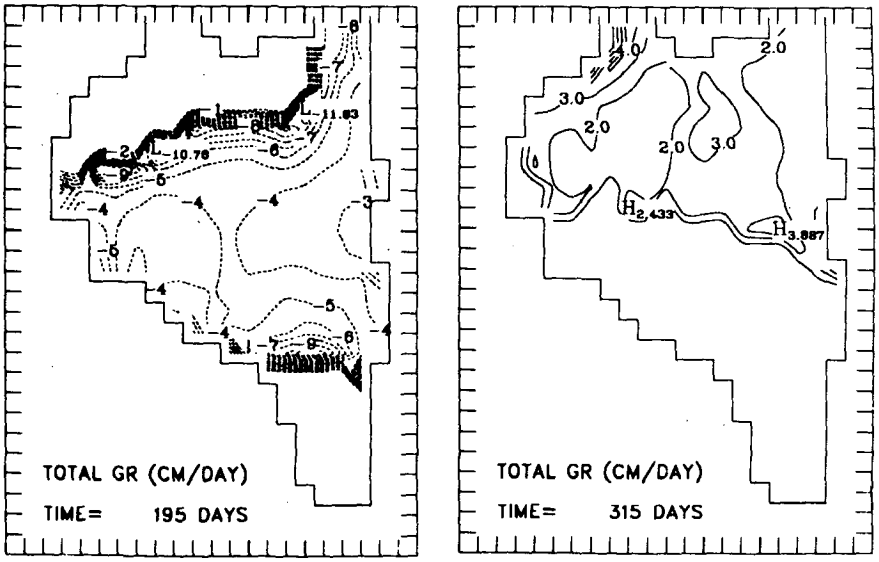

FIG. 10. As in Fig. 8 except for the total growth rate for days 195 (mid-Jul) and 315 (mid-Nov). Contour interval is 0.1 cm day^{-1}.

a coastal current along the east coast transports heat northward from James Bay, and this feature was not simulated in the ocean model.

b. *Melting and freezing processes*

Figure 11 shows in more detail the spatial evolution of the modeled sea ice compactness (concentration) during the melting season. The sea ice breaks up first in James Bay (see day 165, 15 June). Ten days later (25 June), James Bay is nearly ice free, but by contrast the sea ice is just starting to melt in the northwest and is still fairly solid along the south shore of Hudson Bay. This apparent melting in the north only is hypothesized to be due to the strong northwesterly winds that drive ice to the south, where it piles up at a rate greater than the rate of ice reduction due to local heating. On day 185 (5 July), the concentration decreases further in the northwest portion of Hudson Bay and in the northern part of James Bay. On day 195 (mid-July), James Bay is entirely ice free as is the northwest part of Hudson Bay. Sea ice also appears to be advected to the northeast opening by the surface current (see days 185 and 195).

Figure 12 shows a more detailed spatial evolution of the modeled ice compactness in late autumn and early winter—the freezing season. From day 315 (mid-November) to day 335 (5 December), sea ice forms from north to south; however, some open water "leads" occur in the northwest corner. Ten days later (day 345, 15 December), James Bay is still largely ice free, but there is complete ice cover in the northeast part of Hudson Bay. By 25 December (day 355), sea ice has now formed in the eastern half of James Bay. The existence of compactness values less than 9/10 in western James Bay and in the northwestern corner is presumably due to the northwesterly winds that push the locally produced ice offshore. These results are consistent with the observations by Markham (1986) and the satellite measurements by Parkinson (1991). We note that there are well-defined ice edges to the north and south of the ice cover in July (day 195, Fig. 11); there also exists a well-defined ice edge across the middle of Hudson Bay in November (day 315, Fig. 12).

5. Sensitivity study

We have performed a series of sensitivity experiments that involve deleting certain physical processes and changing the values of some parameters, similar to that done by Holland et al. (1991b, 1993). We present below only the results of the more important experiments. Generally speaking, our results were quite consistent with those of Holland et al.

a. *Removal of the oceanic forcing*

To determine the impact of the ocean circulation on sea ice motion in the nearly closed Hudson Bay, we removed the ocean surface circulation and elevation (as shown in Fig. 5) as a forcing mechanism. In mid-April (Fig. 13a) and mid-July (Fig. 13b), the ice motion is to the south and to the southeast, respectively; these motions closely follow the wind patterns for April and July (cf. Fig. 4). In contrast to the observed ice motion and the control run, however, there is no outflow of sea ice in the northeast corner into Hudson Strait because of the lack of ocean current forcing.

b. *Removal of the wind forcing*

According to the observations of Danielson (1969, 1971), Markham (1986), Parkinson (1991), Wang

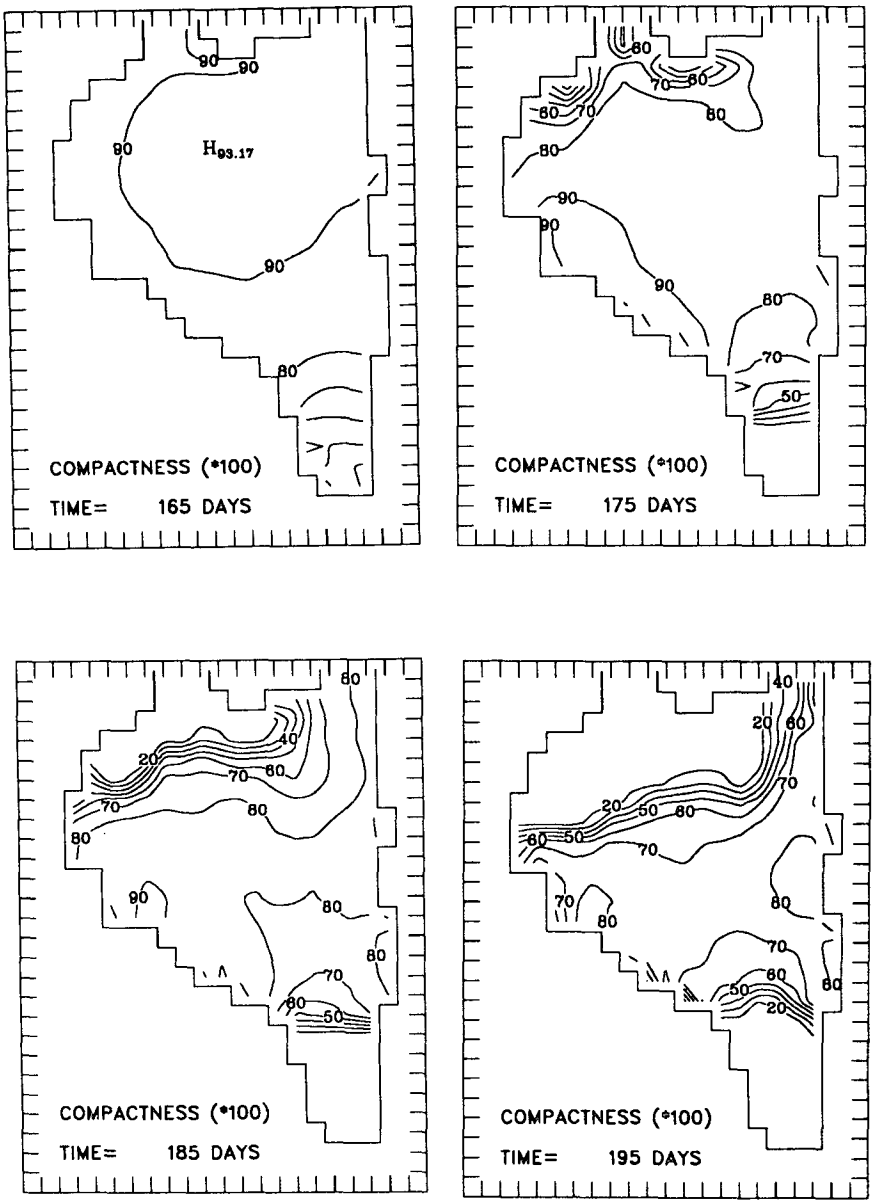

FIG. 11. The spatial distribution of compactness (×100) during the melting season from day 165 (Jun 15) to 195 (Jul 15) in the control run. Contour interval is 10.

(1993), and Wang et al. (1994a), the sea ice piles up along the south shore in mid-July. This appears to result from the strong northerly wind forcing. To test this hypothesis, we removed the wind forcing in this experiment. On day 195 (mid-July) the sea ice does not approach the south shore (see Fig. 13d), but remains in the central part of Hudson Bay, which is quite different from the case in the control run, as shown in Fig. 8 and from observations. Also, we note that in both April (Fig. 13c) and July (Fig. 13d), there is a large amount of ice exported out of Hudson Bay by the ocean currents. These two sensitivity experiments show that sea ice pile-up along the south shore in summer is mainly due to the northwesterly winds and that ice transport out of Hudson Bay is due to the ocean circulation.

c. *Ocean heat flux*

Because of the lack of data for the upward subsurface ocean heat flux, we assumed a flux of $Q_{sea} = 2$ W m^{-2} everywhere in the model domain, similar to what had been used earlier in the modeling of sea ice cover in the Arctic Ocean (Hibler 1979). Thus, it is natural to ask what happens if this flux is doubled or halved, with the other model parameters being

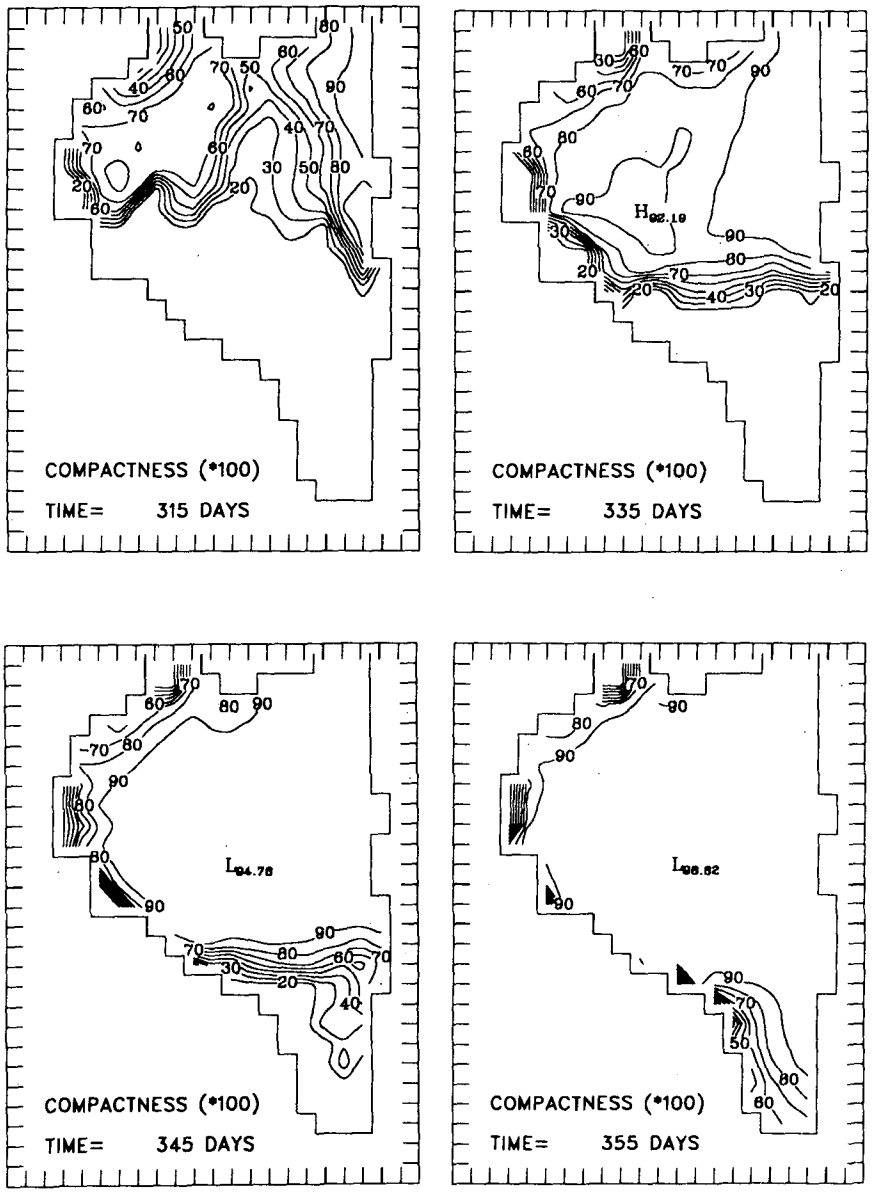

FIG. 12. The spatial distribution of compactness (×100) during the freezing season from day 315 (Nov 15) to 355 (Dec 25) in the control run. Contour interval is 10.

taken to be the same as in the control run. Figure 14 shows the seasonal cycles of the area-averaged ice thickness and mixed layer temperature for $Q_{sea} = 4$ W m^{-2} (upper panels) and for $Q_{sea} = 1$ W m^{-2} (lower panels), with the dashed curve being the control run. We note that doubling (halving) the ocean heat flux results in an advance (delay) in ice melting (cf. the left panels), and thus leads to a higher (lower) mixed layer temperature in summer (right panels). As a consequence of the latter, sea ice forms more slowly or more rapidly in the autumn than in the control run. The difference between the area-averaged thicknesses for the two sensitivity runs is only about 0.02 m, however.

d. *Parameters P* and C*

We carried out the following parameter sensitivity tests on ice strength and the ice strength decay constant [see Eq. (8)]: $P^* = 10 \times 10^3$, 55×10^3 N m^{-2}, and $C = 5$, 20. Figure 15 shows that the ice model with small ice strength ($P^* = 10 \times 10^3$ N m^{-2}, in which case sea ice becomes soft) cannot produce reasonable results in terms of either ice area (Fig. 15a) or thickness

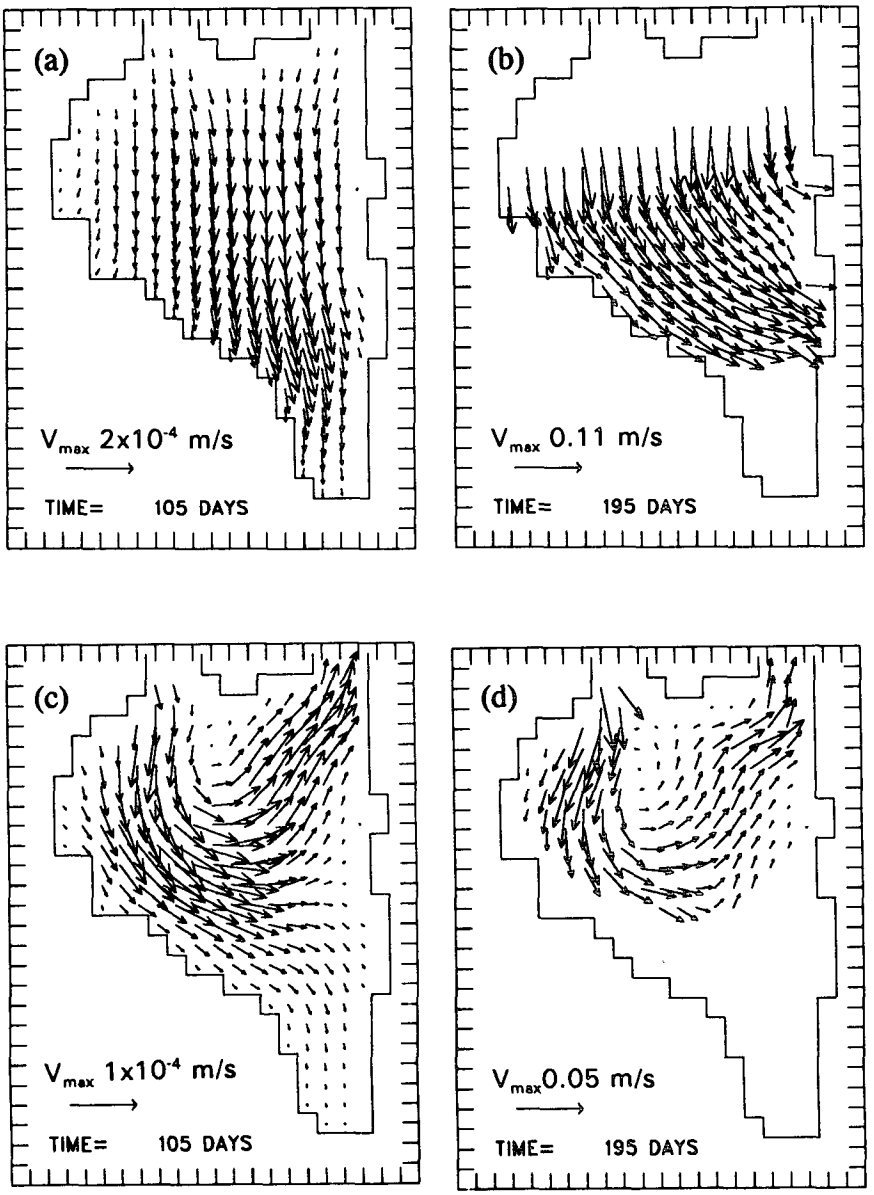

FIG. 13. The sea ice velocity fields for the cases of no ocean current forcing [(a) day 105, (b) day 195], and no wind forcing [(c) day 105, (d) day 195]. Note that the maximum velocity vector is different in each panel.

(Fig. 15b). In particular, the ice is far too thick in eastern Hudson Bay and James Bay, and Hudson Bay never becomes ice free. The maximum winter sea ice velocity is about 10^{-3} m s^{-1}, one order of magnitude greater than in the control run (10^{-4} m s^{-1}, Fig. 8). For $P^* = 55 \times 10^3$ N m^{-2}, the timing of ice melt is delayed, but the sea ice area (Fig. 15a) and thickness distribution (not shown) show little change from the control case.

Figure 16 shows that when C is halved to 5, there is little difference from the control run. But for $C = 20$, the sea ice melts more slowly than in the control run and there is sea ice in summer, contradicting the observations.

Other sensitivity experiments were performed with respect to the remaining parameters listed in Table 1. When small changes were made to those parameters, the results did not change significantly from those in the control run. Also, the results for an f-plane showed little difference from the β-plane results presented above. However, ignoring the Coriolis parameter results in unrealistic ice velocities.

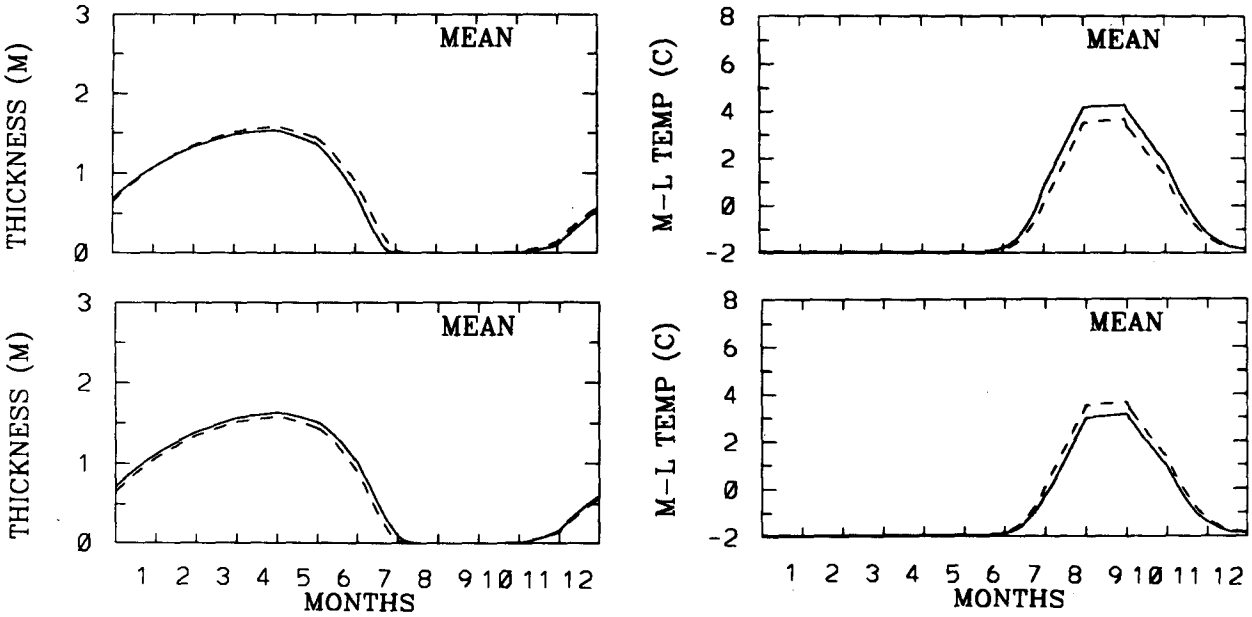

FIG. 14. The seasonal cycles of the area-averaged sea ice thickness and the mixed layer temperature for the ocean heat flux of 4 W m^{-2} (upper panels) and of 1 W m^{-2} (lower panels). The dashed curves correspond to the values from the control run with Q_{sea} = 2 W m^{-2}.

e. Sea ice anomalies due to negative anomalies of surface air temperature

In a data analysis study, Wang et al. (1994a) found that during the first year of an ENSO event, there were negative surface air temperature (SAT) anomalies of about −1°C over Hudson Bay and thus positive anomalies in sea ice area (see their Figs. 8 and 9). During a strong westerly event of the North Atlantic Oscillation, there were negative SAT anomalies of about −1.5°C in winter (see their Figs. 6 and 7) and thus positive anomalies of sea ice area.

To find the model response to a simulated ENSO event, we took the prescribed SAT field as climatology less 1°C everywhere in the domain from February to November in the second year in the model run (the other forcing functions remained the same). Figure 17 shows the resulting anomalies (deviations from the control run) of area-averaged ice thickness and ice cover. The occurrence of positive anomalies in summer and autumn in the model are qualitatively consistent with the observations [see Fig. 8 of Wang et al. (1994a)].

Similarly, to determine the model response to a strong North Atlantic Oscillation event, we took the prescribed SAT as climatology less 2°C everywhere in the domain from first-year December to second-year February (the winter season). Figure 18 shows the second-year anomalies of area-averaged ice thickness and ice cover. We note that the sea ice becomes thicker during winter and remains so until summer. After this, ice conditions return to normal until November. The ice cover area, however, shows little change in the winter due to the boundary constraint (see section 4a); in summer there is a small positive areal anomaly because the thicker ice formed in the previous winter melts more slowly. As a consequence, the mixed layer temperature has a negative anomaly in summer, which results in the earlier formation of ice in the autumn freezing season. This is why in Fig. 18 there are the positive anomalies of both ice thickness and ice area from October to December.

6. Summary and conclusions

We applied Hibler's (1979, 1980) sea ice model to simulate the seasonal cycle of ice cover in Hudson Bay under prescribed realistic climatological monthly atmospheric and winter oceanic forcing. The model is capable of simulating the complete sea ice cover in winter and the ice melting and freezing processes in summer and autumn, respectively. The following conclusions can be drawn:

1) The seasonal cycle of sea ice velocity, compactness, and thickness and growth rate in Hudson Bay appear to be reasonably well reproduced, although a comparison with data is only possible for ice cover and thickness. The complete ice cover in winter and the occurrence of ice-free water in summer are well simulated. Due to the boundary constraint, the sea ice velocity from January to April has a typical magnitude of only $1\text{–}5 \times 10^{-4}$ m s^{-1} (unfortunately, there are no available measurements to confirm this magnitude). However, during the melting and freezing seasons, the

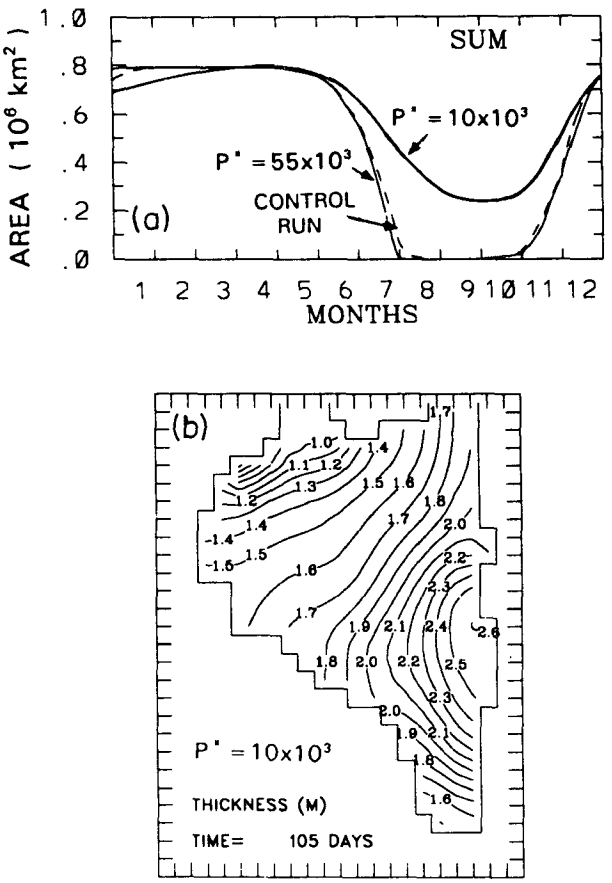

FIG. 15. (a) The seasonal cycle of ice area for cases of P^* = 10 $\times$ 10^3 and 55 $\times$ 10^3 N m^{-2}; the dashed curve denotes the control run for P^* = 27 $\times$ 10^3 N m^{-2} (Fig. 7). (b) The ice thickness field in mid-April for P^* = 10 $\times$ 10^3 N m^{-2}, which should be compared with the control run (Fig. 9).

ice velocity can reach up to 0.15 m s^{-1}, which is a typical speed for the ice motion in the Greenland Sea.

2) The melting and freezing processes have been well simulated. Sea ice breaks up in the early spring in James Bay and continues to melt along the coast.

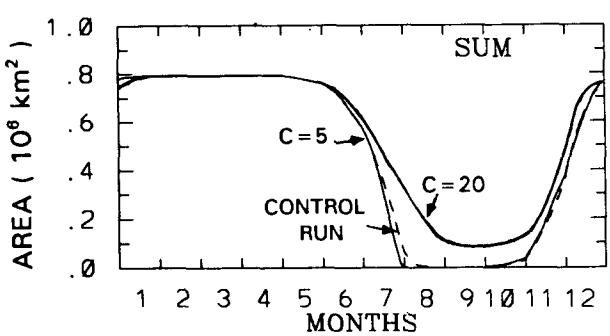

FIG. 16. The seasonal cycle of ice area for the cases of C = 5 and 20. The dashed curve denotes the control run for C = 10 (Fig. 7).

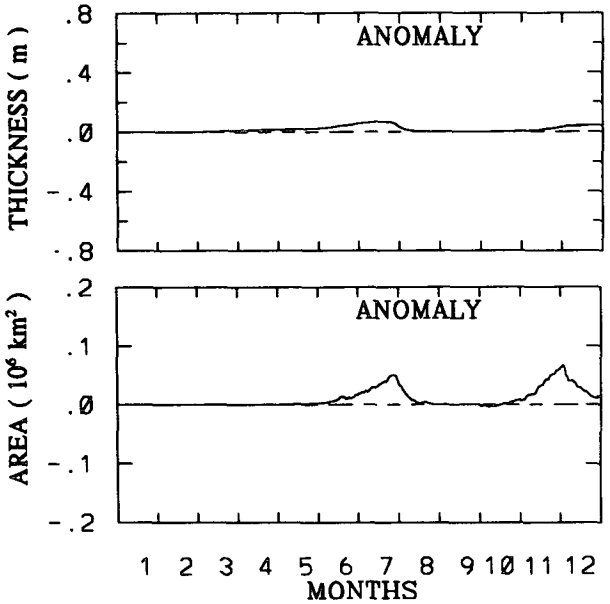

FIG. 17. The anomalies of area-averaged ice thickness and ice-cover area that are produced by imposing a negative anomaly of surface air temperature (1°C lower) from Feb to Nov in the second year of a 2-year run.

However, sea ice melts slowly on the south shore, due to the continuous southward motion of sea ice driven by the wind. In July, sea ice piles up along the south

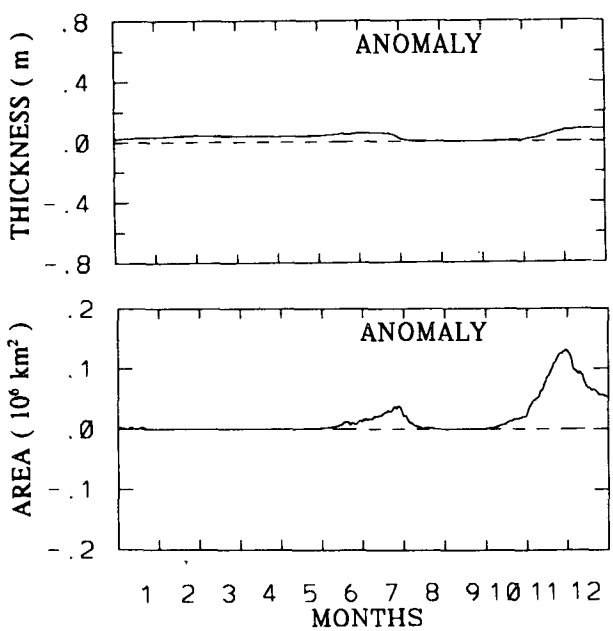

FIG. 18. The second-year anomalies of area-averaged ice thickness and ice cover area produced by imposing a negative anomaly of surface air temperature (2°C lower) from first-year Dec to second-year Feb in a 2-year run.

shore because of the northwesterly winds, a phenomenon which has been observed. Sea ice forms from north to south during autumn and early winter (December), consistent with observations. The timing for both melting and freezing seasons are well simulated. The area-averaged growth rate derived from the model is 1.5–0.5 cm day^{-1} from December to March, negative in May, and reaches its minimum value of about −4 cm day^{-1} (maximum melting rate) in July. During autumn, (the main freezing season) the growth rate ranges from 1 to 2 cm day^{-1}.

3) A sensitivity study shows that the effect of the ocean circulation on the sea ice flow is important in the northeastern part of the bay. In the rest of the domain, realistic wind forcing is the most important external forcing in the simulation.

4) Sea ice anomalies resulting from the imposed negative anomalies of surface air temperature associated with the Southern Oscillation and the North Atlantic Oscillation are found to be qualitatively consistent with the previous observational study of Wang et al. (1994a).

We should emphasize that this simulation was carried out using a sea ice model that was not interactive with the ocean circulation model. Nevertheless, the sea ice simulation results are generally consistent with most of the available observations. But there are some shortcomings of the model and the simulations. We recall that the ocean heat flux for all seasons was fixed equal to 2 W m^{-2} everywhere in the domain. In reality, this heat flux varies spatially and seasonally, but there are no observations of this quantity to check the range of these variations. In addition, the mixed layer depth was fixed to be 25 m. Thus, not surprisingly, there were some discrepancies between the simulated results and observations. For instance, the sea ice in the model does not melt off the east coast of Hudson Bay in mid-July. In addition to the model limitations described above, this particular discrepancy may be partly due to the absence in the model of river runoff during spring and summer. Because the runoff water temperature is normally higher than those of the ice temperature and offshore waters along the east coast of Hudson Bay, such river runoff would enhance ice melt. Furthermore, heat advection by the coastal current along the eastern shore, which is neglected in the simulation, may be important in the melting season, according to Hibler and Bryan (1987). The above, and other discrepancies, would probably be further minimized with the use of a fully coupled ice–ocean model that has warm river runoff and advection of heat northward along the eastern shore during the melting season.

Acknowledgments. We are indebted to Dr. W. D. Hibler III for supplying the sea ice model, Drs. A. F. Blumberg and G. L. Mellor for supplying the ocean model, and J. E. Walsh for supplying the sea ice and sea level pressure dataset. JW thanks Drs. S. Prinsenberg, M. Ikeda, and C. Tang for discussions on the ice flow in Hudson Bay and on sea ice numerical modeling. We also thank two anonymous reviewers for their constructive and helpful comments on a first version of this paper. This study was supported by research grants from NSERC and Fonds FCAR awarded to LAM and RGI, and by an AES science subvention awarded to LAM.

REFERENCES

Blumberg, A. F., and G. L. Mellor, 1983: Diagnostic and prognostic numerical circulation studies of the South Atlantic Bight. *J. Geophys. Res.*, **88,** 4579–4592.

——, and ——, 1987: A description of a three-dimensional coastal ocean circulation model. *Coastal and Estuarine Sciences 4: Three-Dimensional Coastal Ocean Models,* N. S. Heaps, Ed., Amer. Geophys. Union, Washington D.C., 1–16.

Cheng, A., and R. Preller, 1992: An ice–ocean coupled model for the northern hemisphere. *Geophys. Res. Lett.*, **19,** 901–904.

Danielson, E. W., Jr., 1969: The surface heat budget of Hudson Bay. Marine Sciences Manuscript Rep. No. 9, Marine Sciences Centre, McGill University, Montreal, 196 pp.

——, 1971: Hudson Bay ice conditions. *Arctic,* **24,** 90–107.

Fleming, G. H., and A. J. Semtner Jr., 1991: A numerical study of interannual ocean forcing on Arctic ice. *J. Geophys. Res.*, **96,** 4589–4603.

Häkkinen, S., and G. L. Mellor, 1990: One hundred years of Arctic ice cover variations as simulated by a one-dimensional, ice-ocean model. *J. Geophys. Res.*, **95,** 15 959–15 969.

——, ——, and L. Kantha, 1992: Simulation of deep convection in the Greenland Sea. *J. Geophys. Res.*, **97,** 5389–5408.

Hibler III, W. D., 1979: A dynamic thermodynamic sea ice model. *J. Phys. Oceanogr.*, **9,** 815–846.

——, 1980: Modeling a variable thickness sea ice cover. *Mon. Wea. Rev.*, **108,** 1943–1973.

——, and K. Bryan, 1987: A diagnostic ice–ocean model. *J. Phys. Oceanogr.*, **17,** 987–1015.

——, and J. E. Walsh, 1982: On modeling seasonal and interannual fluctuations of Arctic sea ice. *J. Phys. Oceanogr.*, **12,** 1514–1523.

Holland, D. M., L. A. Mysak, and J. M. Oberhuber, 1991a: Simulation of the seasonal Arctic sea ice cover with a dynamic thermodynamic sea ice model. C^{2}GCR Rep. No. 91-17, McGill University, Montreal, 68 pp.

——, ——, and ——, 1991b: Sensitivity study of a dynamic thermodynamic sea ice model. C^{2}GCR Rep. No. 91-18, McGill University, Montreal, 305 pp.

——, ——, D. K. Manak, and J. M. Oberhuber, 1993: Sensitivity study of a dynamic thermodynamic sea ice model. *J. Geophys. Res.*, **98,** 2561–2586.

Ikeda, M., 1985: A coupled ice-ocean model of a wind-driven coastal flow. *J. Geophys. Res.*, **90,** 9119–9128.

——, 1988: A three-dimensional coupled ice–ocean model of coastal circulation. *J. Geophys. Res.*, **93,** 10 731–10 748.

——, 1991a: Numerical modeling of ocean circulation and ice cover over the continental shelf. *J. Phys. Oceanogr.*, **21,** 97–117.

——, 1991b: Wind-induced mesoscale features in a coupled ice–ocean system. *J. Geophys. Res.*, **96,** 4623–4629.

Kantha, L., and G. L. Mellor, 1989: A two-dimensional coupled ice–ocean coupled model of the Bering Sea marginal ice zone. *J. Geophys. Res.*, **94,** 10 921–10 935.

Lemke, P., W. B. Owens, and W. D. Hibler III, 1990: A coupled sea ice–mixed layer–pycnocline model for the Weddell Sea. *J. Geophys. Res.*, **95,** 9513–9525.

Manabe, S., K. Bryan, and M. J. Spelman, 1979: A global ocean–atmosphere climate model with seasonal variation for future studies of climate sensitivity. *Dyn. Atmos. Ocean,* **3,** 393–426.

Markham, W. E., 1981: *Ice Atlas of Canadian Arctic Waterways.* Environment Canada Atmospheric Environment Service, 198 pp.

——, 1986: The ice cover. *Canadian Inland Seas,* I. P. Martini, Ed., Elsevier, 101–116.

Mellor, G. L., and L. Kantha, 1989: An ice-ocean coupled model. *J. Geophys. Res.,* **94,** 10 937–10 954.

Mysak, L. A., and D. K. Manak, 1989: Arctic sea-ice extent and anomalies, 1953–1984. *Atmos.–Ocean,* **27,** 376–405.

Overland, J. E., and C. H. Pease, 1988: Modeling ice dynamics of coastal seas. *J. Geophys. Res.,* **93,** 15 619–15 637.

Parkinson, C. L., 1991: Interannual variability of the spatial distribution of sea ice in the north polar region. *J. Geophys. Res.,* **96,** 4791–4801.

——, and D. J. Cavalieri, 1989: Arctic sea ice 1973–87: Seasonal, regional, and interannual variability. *J. Geophys. Res.,* **94,** 14 499–14 523.

——, and W. M. Washington, 1979: A large-scale numerical model of sea ice. *J. Geophys. Res.,* **84,** 311–337.

Piacsek, S., R. Allard, and A. Warn-Varnas, 1991: Studies of the Arctic ice cover and upper ocean with a coupled ice-ocean model. *J. Geophys. Res.,* **96,** 4631–4650.

Prinsenberg, S. J., 1984: Freshwater contents and heat budgets of James Bay and Hudson Bay. *Contin. Shelf Res.,* **3,** 191–200.

——, 1986: The circulation pattern and current structure of Hudson Bay. *Canadian Inland Seas,* I. P. Martini, Ed., Elsevier, 187–204.

——, 1988: Ice-cover and ice-ridge contributions to freshwater contents of Hudson Bay and Foxe Basin. *Arctic,* **41,** 6–11.

——, and I. K. Peterson, 1992: Sea ice properties off Labrador and Newfoundland during LIMEX'89. *Atmos.–Ocean,* **30,** 207–222.

Ramming, H., and Z. Kowalik, 1980: *Numerical Modelling of Marine Hydrodynamics: Applications to Dynamic Physical Processes.* Elsevier, 368 pp.

Riedlinger, S. H., and R. H. Preller, 1991: The development of a coupled ice-ocean model for forecasting ice conditions in the Arctic. *J. Geophys. Res.,* **96,** 16 955–16 977.

Semtner, A. J., Jr., 1976: A model for the thermodynamic growth of sea ice in numerical investigations of climate. *J. Phys. Oceanogr.,* **6,** 379–389.

——, 1987: A numerical study of sea ice and ocean circulation in the Arctic. *J. Phys. Oceanogr.,* **17,** 1077–1099.

Tang, C. L., 1991: A two-dimensional thermodynamic model for sea ice advance and retreat in the Newfoundland marginal ice zone. *J. Geophys. Res.,* **96,** 4723–4737.

——, and D. B. Fissel, 1991: A simple ice-ocean coupled model for ice drift in marginal ice zones. *J. Mar. Sys.,* **2,** 465–475.

Titus, R. L., 1967: *Upper Air Climate of Canada: Charts and Monthly Geopotential, Temperature and Humidity 1951–60.* Meteorol. Branch, Dept. of Transport, Toronto, Ontario, 103 pp.

Walsh, J. E., and C. M. Johnson, 1979a: An analysis of sea ice fluctuations, 1953–77. *J. Phys. Oceanogr.,* **9,** 580–591.

——, and ——, 1979b: Interannual atmospheric variability and associated fluctuations in Arctic sea ice extent. *J. Geophys. Res.,* **84,** 6915–6928.

——, and W. L. Chapman, 1990: Short-term climate variability of the Arctic. *J. Climate,* **3,** 237–250.

Wang, J., 1993: Interannual variability of sea-ice cover in Hudson Bay, Baffin Bay, and the Labrador Sea, and numerical simulation of ocean circulation and sea ice cover in Hudson Bay. Ph.D. thesis, McGill University, 162 pp. [Available as C-GCR Rep. No. 93-2, McGill University.]

——, L. A. Mysak, and R. G. Ingram, 1994a: Interannual variability of sea-ice cover in Hudson Bay, Baffin Bay and the Labrador Sea. *Atmos.–Ocean,* **32,** 421–447.

——, ——, and ——, 1994b: A three-dimensional numerical simulation of Hudson Bay summer ocean circulation: topographic gyres, separations, and coastal jets. *J. Phys. Oceanogr.,* **24,** 2496–2514.

Yao, T., and M. Ikeda, 1990: A model of sea ice and the upper ocean mixed layer off Labrador. *J. Geophys. Res.,* **95,** 11 603–11 612.